Journal of Applied Physics

RESEARCH ARTICLE | MARCH 24 2026

Spin wave dispersion of the van der Waals antiferromagnet $NiPS_3$

Ritesh Das ; Rob den Teuling ; Artem V. Bondarenko ; Elena V. Tartakovskaya; Gerrit E. W. Bauer ; Jaime Ferrer ; Yaroslav M. Blanter

J. Appl. Phys. 139, 123902 (2026)
https://doi.org/10.1063/5.0312007

Journal of Applied Physics ARTICLE pubs.aip.org/aip/jap

Spin wave dispersion of the van der Waals antiferromagnet $NiPS_3$

Cite as: J. Appl. Phys. **139**, 123902 (2026); doi: 10.1063/5.0312007
Submitted: 13 November 2025 · Accepted: 2 March 2026 ·
Published Online: 24 March 2026

View Online Export Citation CrossMark

Ritesh Das,[1,a)] Rob den Teuling,[1] Artem V. Bondarenko,[1] Elena V. Tartakovskaya,[1,2,3] Gerrit E. W. Bauer,[4,5] Jaime Ferrer,[6,7] and Yaroslav M. Blanter[1,b)]

AFFILIATIONS

[1]Kavli Institute of Nanoscience, Delft University of Technology, Lorentzweg 1, 2628 CJ Delft, The Netherlands
[2]V.G. Baryakhtar Institute of Magnetism of the NAS of Ukraine, 36b Vernadsky Boulevard, 03142 Kiev, Ukraine
[3]Institute of Spintronics and Quantum Information, Faculty of Physics and Astronomy, Adam Mickiewicz University, Poznań, Uniwersytetu Poznańskiego 2, 61-614 Poznań, Poland
[4]WPI Advanced Institute for Materials Research and IMR and CSIS, Tohoku University, Sendai, Japan
[5]Kavli Institute for Theoretical Sciences, University of the Chinese Academy of Sciences, Beijing, China
[6]Departamento de Fisica, Universidad de Oviedo, 33007 Oviedo, Spain
[7]Centro de Investigacion en Nanomateriales y Nanotecnologia, Universidad de Oviedo-CSIC, 33940 El Entrego, Spain

[a)]**Author to whom correspondence should be addressed:** R.D.Das@tudelft.nl
[b)]**Electronic mail:** Y.M.Blanter@tudelft.nl

ABSTRACT

We calculate the magnon dispersion spectra of the two-dimensional zigzag van der Waals antiferromagnet $NiPS_3$ for monolayer, bilayer, and bulk systems as a function of an external magnetic field. We compare the exchange and anisotropy constants of a spin model as calculated by first principles with those obtained experimentally. We can accurately explain the transition from a collinear to a canted ground state for a magnetic field applied normal to the (in-plane) easy-axis and a spin-flop transition when the field is parallel to it. A topologically protected Dirac nodal line is present and robust with respect to both external and anisotropy fields.

I. INTRODUCTION

The elementary excitations of a magnetic ground state are known as magnons, the quanta of spin waves,[1–5] that are ubiquitous in magnetometry[6,7] and caloritronics,[8–10] and have potentially useful applications in computation.[5,11] They are compatible with complementary metal–oxide–semiconductor (CMOS) technology for logic devices,[5] and the information transmitted by spin waves does not suffer from Ohmic losses.[5]

Promising platforms for studying spin waves are two-dimensional (2D) van der Waals (vdW) magnetic materials.[12–15] 2D vdW magnets can be exfoliated to monolayers or a few layers.[13,16] The competing energies in these materials give rise to highly tunable magnon dispersions and spin-wave dynamics.[14,17] $NiPS_3$ is a vdW antiferromagnet with a hexagonal zigzag ground state, where the spins are predominantly in-plane along an easy-axis,[18–22] with a small out-of-plane component.[20,21] $NiPS_3$ has been predicted to host quantum phenomena, such as non-trivial topology,[23] anomalous scattering,[21] and non-trivial magnetic order.[16] To describe these effects, a clear understanding of the Hamiltonian and spin-wave dynamics in $NiPS_3$ is essential.

Spin waves in $NiPS_3$ have been studied in bulk samples through neutron scattering experiments,[19–21] which provide dispersions across the entire Brillouin zone. Several models describe the magnon dispersions in monolayer[19] and bulk $NiPS_3$ samples,[19–21] but outstanding questions remain, such as the dependence on externally applied magnetic fields, crystal anisotropy constants, and number of layers. According to the Mermin–Wagner theorem, a Heisenberg magnet cannot exhibit long-range magnetic order in the 2D limit without anisotropy.[24] Although all models of $NiPS_3$ predict easy-axis anisotropy, long-range magnetic order exists only in bilayer samples and vanishes in monolayers.[16] This suggests that interlayer exchange is crucial for maintaining long-range order.

The bilayer model is, therefore, a minimal model for studying low-dimensional antiferromagnetism in many vdW systems. Recent observation of the spin resonance in bilayer $NiPS_3$[25,26] makes a model for the bilayer particularly relevant.

In this work, we compute the magnon dispersion of monolayer and bilayer $NiPS_3$ by solving the Landau–Lifshitz (LL) equation analytically under specific conditions and numerically in the general case. We adopt an in-plane zigzag antiferromagnetic ground state as established by prior neutron scattering experiments on bulk $NiPS_3$.[19–21] For the monolayer, we determine the exchange and anisotropy constants from first-principles calculations, which confirm this ground state. Since first-principles methods are not as accurate for bilayer and bulk van der Waals materials due to the weak interlayer interactions, we adopt exchange parameters derived from neutron scattering measurements for these cases. Motivated by recent experimental interest in the magnetic resonance of bilayer van der Waals magnets,[25,27] we present, to the best of our knowledge, the first analytic treatment of bilayer $NiPS_3$ that incorporates field-induced symmetry breaking and interlayer exchange. We address field-induced phase transitions and magnon dispersion relations in non-collinear zigzag antiferromagnets, reveal band degeneracies that persist under varying fields, anisotropy, and layer number, and predict a magnon Hanle effect in non-collinear phases. We also investigate the presence of Dirac nodal lines—magnon bands that cross along a line in specific directions in the Brillouin zone. These "Dirac nodal lines"[23,28,29] host topological magnons[23,28,29] and lead to chiral edge states.[28] Analytic expressions of the magnon band structure, using first-principles parameters for the monolayer and neutron-scattering-based parameters for the bilayer and bulk, provide a foundation for interpreting future neutron, photoluminescence, and spin transport experiments in $NiPS_3$.

This paper is organized as follows: In Sec. II, we elaborate on the model and describe the Hamiltonian governing the ground state and its excitations. We show how to linearize the Landau–Lifshitz equation (LL equation) to compute spin wave dispersion. In Sec. III, we describe the first-principles methods used to compute the exchange and anisotropy constants. In Sec. IV, we present the magnon dispersion for monolayer and bilayer $NiPS_3$, examining the dependence of the spin-wave band structure on external fields and anisotropy constants. In Sec. V, we report the resonance frequencies as a function of applied magnetic field. We conclude in Sec. VI.

II. MODEL

The magnetic structure of $NiPS_3$ in the crystallographic unit cell, along with the corresponding Brillouin zone, is shown in Fig. 1. $NiPS_3$ features a hexagonal zigzag antiferromagnetic lattice,[18–21,23] with magnetic moments localized on the Ni atoms. Recent neutron scattering experiments by Lançon *et al.*[19] and Wildes *et al.*[20] have proposed two similar yet conflicting models for the magnetic structure of $NiPS_3$. A key difference between Refs. 19 and 20 lies in the form of the spin Hamiltonian used to analyze the neutron scattering data. In Ref. 19, the fitted Hamiltonian includes an easy-axis anisotropy but does not incorporate a hard-axis term. As a result, Ref. 19 reports a strong easy-axis along a single

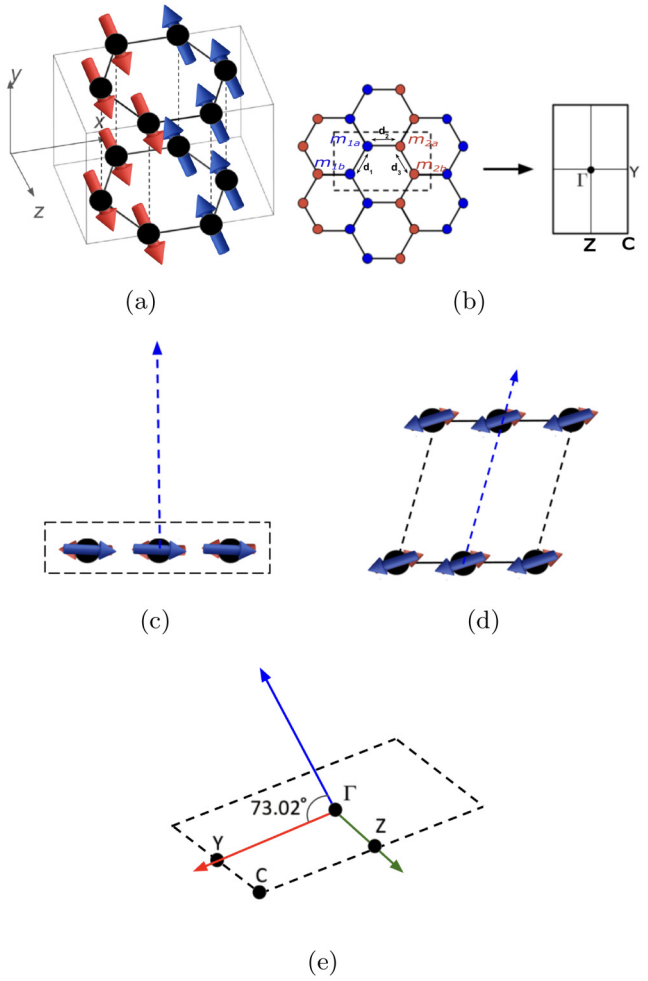

FIG. 1. (a) Bilayer $NiPS_3$ assumes a zigzag antiferromagnetic hexagonal lattice with in-plane magnetic moments. Red arrows represent spin-up (along z) and blue arrows represent spin-down directions. (b) Unit cell in real space (left) and the corresponding Brillouin zone in reciprocal space (right). The red dots represent spin-up and blue dots spin-down magnetic moments. (c) shows the ground state in a monolayer found via density functional theory (DFT) calculations. (d) illustrates the observed magnetic structure in bulk[20] with a hard-axis at an angle of 73.02° with the plane and a ground state in which spins are pulled slightly out-of-plane. (e) Shows the orientation of the hard-axis (in blue) in the reciprocal space.

in-plane direction, resulting in spins that are confined to the plane in the ground state [see Fig. 1(a)]. In this model, the spins lie along the z axis. The $x(y)$ axis is perpendicular to the z axis and corresponds to the direction in (out of) the crystallographic plane. In contrast, Ref. 20 explicitly includes both easy-axis and hard-axis anisotropies, allowing for a more general description of the magnetic anisotropy in $NiPS_3$. Reference 20 finds a weak easy-axis along the z-direction, along with a strong out-of-plane hard-axis making an angle of 73.02° with the plane. This results in the spins

lying slightly out-of-plane in the ground state [see Fig. 1(d)]. The model proposed in Ref. 20 is more recent and is considered to provide a more accurate description of the magnetic structure. Reference 21 also finds values that agree with Ref. 20.

The reason for the canted hard-axis in the bilayer and bulk is the stacking of $NiPS_3$ layers, which affects the magnetic anisotropy and ground state magnetization direction. The symmetry of the monolayer [Fig. 1(c)] forces the hard-axis to lie perpendicular to the plane. In contrast, in the ground state of the bilayer [Fig. 1(d)], the relative shift of the monolayers breaks the axial symmetry and cants the hard-axis by a significant angle from the film normal.

For simplicity, we adopt a model with both an easy and a hard-axis,[20] assuming that the hard-axis is perfectly perpendicular to the plane (rather than at the observed angle of 73.02°). This simplification results in a ground state where the spins lie entirely in the plane. Note that our first-principles calculations (see Sec. III) also fail to find the observed slightly out-of-plane configuration in the monolayer. The magnetic primitive unit cell contains four atoms in a rectangular parallelepiped, as depicted in Fig. 1(b) together with the first Brillouin zone. In Subsections II A and II B, we specify the Hamiltonian and determine the ground state by minimizing the corresponding free energy. The Landau–Lifshitz (LL) equation is then derived by linearizing the free energy for small excitations around the ground state, from which we calculate the spin-wave dispersion for various system parameters.

We model the system using a Heisenberg Hamiltonian that incorporates the magnetocrystalline anisotropy, the Zeeman energy from an applied external field, and the exchange interaction up to the next-next nearest neighboring spins. The anisotropy and exchange parameters are determined from first-principles calculations, except for the interlayer exchange.

A. Hamiltonian

We proceed from the Heisenberg Hamiltonian[19,20]

$$H = -\sum_{j,\sigma} \mathcal{J}_{jj+\sigma} \vec{S}_j \cdot \vec{S}_{j+\sigma} - \sum_{n,j} \mathcal{D}_n \left(S_j^n\right)^2 - \sum_j \gamma\hbar \vec{S}_j \cdot \vec{B}_0, \tag{1}$$

where $\vec{S}_j$ is the spin (in units of $\hbar$) at the lattice point j, S_j^n is the component of the spin at lattice point j along the n axis ($n \in x, y, z$), $\mathcal{J}_{jj+\sigma}$ is the exchange interaction between spins at lattice points j and $j+\sigma$, and $\mathcal{D}_n$ is the strength of the uniaxial anisotropy constant in the direction normal to the lattice planes along the n axis. $\vec{B}_0$ is an external magnetic field that can be applied in any general direction that is in the plane, and γ is the gyromagnetic ratio given by $\gamma/2\pi = 28$ GHz/T. Each side of the honeycomb is of length l_a, and the distance between two atoms on top of each other in different layers is l_b. In this work, we only look at an external field applied along the z axis and the x axis. The zigzag configuration emerges when taking the exchange interaction up to the next-next-nearest neighbor into account. The resulting Hamiltonian for a magnetic monolayer with exchange interaction

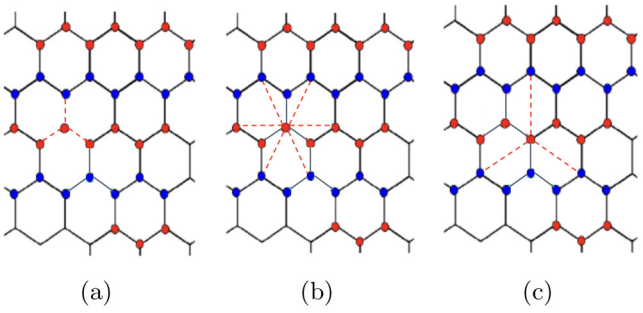

FIG. 2. Exchange interactions in $NiPS_3$. The red (blue) dots represent spin-up (spin-down) local moments. The black lines denote the bonds in the crystal, and the red dashed lines denote the path to the (a) nearest neighbors, (b) next-nearest neighbors, and (c) next-next-nearest neighbors.

up to the next-next-nearest neighbor into account is given by

$$\begin{aligned} H_{mono} = &-\sum_{j,\sigma_1} \mathcal{J}_1 \vec{S}_j \cdot \vec{S}_{j+\sigma_1} - \sum_{j,\sigma_2} \mathcal{J}_2 \vec{S}_j \cdot \vec{S}_{j+\sigma_2} \\ &- \sum_{j,\sigma_3} \mathcal{J}_3 \vec{S}_j \cdot \vec{S}_{j+\sigma_3} - \sum_j \mathcal{D}_z \left(S_j^z\right)^2 - \sum_j \mathcal{D}_y \left(S_j^y\right)^2 \\ &- \sum_j \mathcal{D}_x \left(S_j^x\right)^2 - \sum_j \gamma\hbar \vec{S}_j \cdot \vec{B}_0, \end{aligned} \tag{2}$$

where $\mathcal{J}_i$ is the ith nearest-neighbor exchange between spins on lattice sites j and $j+\sigma_i$. The nearest, next-nearest, and next-next-nearest neighbors are shown in Fig. 2. $\vec{S}_{j+\sigma_i}$ represents the spin of the ith nearest neighbor of $\vec{S}_j$. The numerical values for the exchange coupling and anisotropy found through neutron scattering experiments[19,20] and DFT are given in Table II.

B. Landau–Lifshitz equation

We investigate the spin dynamics by the Landau–Lifshitz (LL) equation[3,30]

$$\frac{d\vec{m}_j(t)}{dt} = -\gamma \left[\vec{m}_j(t) \times \vec{H}_{eff}(t)\right], \tag{3}$$

where $\vec{m}_j = \gamma\hbar \vec{S}_j / M_s$[3,31] is the local magnetic moment at lattice site j. The local magnetic moments are treated as classical vectors with constant magnitude. The effective field $\vec{H}_{eff}$ for the magnetization in each sublattice is derived by taking the functional derivative[3,31]

$$\vec{H}_{eff,j} = \frac{1}{\mu_0 M_s} \frac{\partial \epsilon}{\partial |m_j|}, \tag{4}$$

where the energy density per unit cell ϵ is derived from the Hamiltonian in Eq. (1) by substituting the quantum spin operators

with the corresponding classical magnetization amplitudes:[3,31]

$$\epsilon/M_s = -\sum_{j,\sigma} J_{j,j+\sigma}\vec{m}_j \cdot \vec{m}_{j+\sigma} - \sum_{j,n} D_n\left(m_j^n\right)^2 - \sum_j \vec{m}_j \cdot \vec{B}_0, \tag{5}$$

where M_s is the saturation magnetization, $J_i = \mathcal{J}_i S/\gamma\hbar$, $D_n = \mathcal{D}_n S/\gamma\hbar$, and the index j goes over all lattice sites in the unit cell. Ni has two holes in the 3d shell, so its spin $S = M_s/\gamma\hbar = 1$.

The LL equation is linear in the spin-wave approximation. For a spin aligned along the z axis in its ground state, the dynamic magnetization of its excited state is written in the spin-wave approximation as[3,31]

$$\vec{m}_j = m_j^z\hat{z} + \left(m_j^x\hat{x} + m_j^y\hat{y}\right)e^{i(\omega t - k_x x_j - k_y y_j - k_z z_j)}, \tag{6}$$

where $\vec{m}_j$ is the magnetization vector, m_j^n is the component of the magnetization along the n axis at lattice site j. Furthermore, k_n is the component of the wavevector along the n axis. The spatial coordinates x_j, y_j, and z_j can only take discrete values corresponding to the lattice sites j. Using Eq. (6), the LL equation is linearized using a standard procedure.[31]

In the ground state, the spins form two sublattices (see Fig. 1). For a field applied in-plane, the ground state is canted and fully described by the azimuthal angles θ_1 and θ_2 made with the intermediate axis by the spins of spin-up sublattices and spin-down sublattices, respectively. The classical energy in the ground state follows from Eq. (5) by assuming that the sublattice magnetizations are constant classical vectors with canting angles θ_1 and θ_2 relative to the z axis[31] and is given by

$$\begin{aligned}\epsilon_{gs} = M_s\big[&-D_x\cos^2\theta_1 - D_x\cos^2\theta_2 - D_z\sin^2\theta_1\\ &-D_z\sin^2\theta_2 - B_0\sin\theta_1 - B_0\sin\theta_2 - J_f\\ &-J_{af}(\sin\theta_1\sin\theta_2 - \cos\theta_1\cos\theta_2)\big].\end{aligned} \tag{7}$$

Here, $J_{af} = J_1 + 4J_2 + 3J_3$, and $J_f = 2J_1 + 2J_2$. We consider first the easiest case of the magnetic field applied along the easy-axis. The ground state is found by minimizing the energy in Eq. (7) with respect to the angles θ_1 and θ_2,[31] resulting in the antiferromagnetic state [see Fig. 3(a)], $\theta_1 = -\theta_2 = \pi/2$ for $B_0 < B_c = 2\sqrt{(D_z - D_x)(D_x - D_z - J_{af})}$, and the spin-flop state [see Fig. 3(b)] given by $\theta_1 = \theta_2 = \theta_{sf}$, where θ_{sf} is given by[31]

$$\sin\theta_{sf} = \frac{B_0}{2(D_x - D_z - J_{af})}. \tag{8}$$

When the magnetic field is applied along the intermediate axis, the spins are in a canted state. In the canted state, the spins make an angle θ_c with the easy-axis [see Fig. 3(c)]. The angle θ_c is given by[31]

$$\sin\theta_c = \frac{B_0}{2(D_z - D_x - J_{af})}. \tag{9}$$

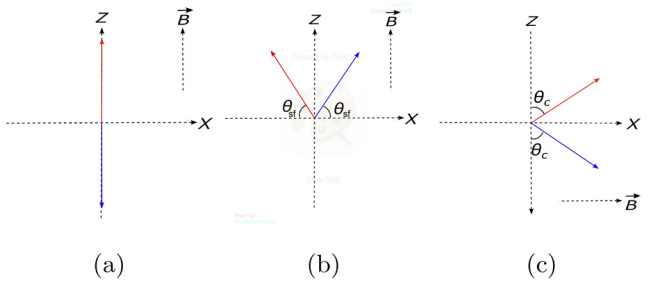

FIG. 3. Ground state magnetic configurations of an antiferromagnet with two sublattices. The easy-axis is along z, and the x axis is in-plane and perpendicular to the z axis. The y axis is out-of-plane. The red arrow indicates the spins in sublattice 1, and the blue arrow indicates the spins in sublattice 2. (a) The antiferromagnetic ground state when no magnetic field or a weak external magnetic field is applied along the easy-axis. (b) The ground state in the spin-flop phase occurs beyond a critical value for the magnetic field. (c) The magnetic moments aligned in the canted phase, which occurs when a magnetic field is applied along the intermediate axis.

In Sec. III, we describe the first-principles methods used to compute the exchange and anisotropy constants for our model.

III. FIRST-PRINCIPLES CALCULATIONS

We have carried out first-principles simulations of several magnetic phases of monolayer $NiPS_3$ by the Density Functional Theory (DFT) code SIESTA.[32] These simulations have been carried out using the Perdew–Burke–Ernzerhof generalized gradient approximation exchange-correlation density functional[33] and include the full spin–orbit interaction self-consistently[34] and optimized pseudopotentials[35] and the triple-zeta double polarized basis set with an energy shift of 10 meV; this is a very complete basis having long radia. We used stringent accuracy parameters for the real-space integrals (1000 Rydberg) and reciprocal-space sums ($30 \times 30 \times 1$ k points) allowing tolerances for the Hamiltonian and density matrix elements of 10^{-5} meV and 10^{-6}, respectively. We relaxed all inter-atomic forces to below 10^{-3} eV/A depending on the ground state, allowing the unit cell stresses and pressures to below 0.005 GPa. We have simulated four magnetic phases with spins aligned along the z axis. These correspond to ferromagnetic and Néel antiferromagnetic alignments, as well as the so-called zigzag and stripy phases, where spins are aligned antiferromagnetically along the zigzag/armchair directions and vice versa. No ferromagnetic phase could be converged. The zigzag phase is energetically favored by about 40 meV over the next most stable state, the Néel AFM. In all four phases, the ground state spins ended up completely in-plane. We have simulated also x- and y-axis-oriented zigzag phases. The x-axis zigzag phase is almost degenerate to the z-axis zigzag phase, while the y axis zigzag is 0.15 meV higher in energy. These two phases have a slightly higher energy of about 0.5 meV, reflecting a small spin–orbit-driven magnetic anisotropy. We picked the Hamiltonian of the stable z-axis zigzag phase and used our post-processing tool Grogu,[36] which

TABLE I. Change in bond lengths (in Å) due to magnetic order.

Magnetic order	Δd_1 (Å)	Δd_2 (Å)	Δd_3 (Å)
Zigzag	0.011	−0.006	0.011
Néel	−0.010	−0.012	−0.010

determines the exchange and intra-atomic anisotropy tensors of a given magnet to any desired neighbor shell using pertubation theory.

While an ideally easy-plane 2D magnet can support only quasi-long-range order, the small in-plane easy-axis anisotropy of $NiPS_3$ stabilizes antiferromagnetism at low temperatures. To confirm the long-range order, we run Monte Carlo simulations with the Metropolis algorithm[37] on a finite $32 \times 24 \times 1$ lattice of $NiPS_3$ at 0.1 K (see Fig. 13 in Appendix E). Even for this finite system, we find robust zigzag ordering consistent with experimental observations and theoretical expectations.[18,19,23] The extrapolation to the thermodynamic limit is beyond the scope of the present paper, but similar systems sizes have been used previously by others.[38]

The magnetic order is associated with magnetostrictive symmetry-breaking lattice distortions.[39] Table I shows the change in bond lengths for different magnetic orders relative to the paramagnetic state with $d_1 = d_2 = d_3 = 3.387$ Å [see Fig. 1(b)]. The distortions are anisotropic for the zigzag state, resulting in an easy-axis magnetic anisotropy. The anisotropy induced by lattice distortions constitutes an essential component of the Hamiltonian in Eq. (2) and plays a key role in determining both the magnetic ground state and the resulting magnon dispersion.

Our code Grogu[36] computes the exchange constants by the LKAG (Liechtenstein, Katsnelson, Antropov, and Gubanov) method.[40] This method determines the exchange tensor J_{ij} between two given magnetic atoms by the energy change due to rotations of the two spins, repeating the procedure for all pairs within a large enough cut-off distance. Analogously, the magnetic anisotropy tensor follows from the energy costs of separately rotating all single spins in the unit cell. The code considers the spin–orbit interaction self-consistently and has been thoroughly tested for a range of two-dimensional materials.[41–44]

Table II compares the computed exchange and anisotropy constants with experimental values from Refs. 19 and 20. In agreement with these previous studies, we find a large antiferromagnetic next-next-nearest neighbor exchange, a ferromagnetic and intermediate nearest-neighbor exchange, and a small next-nearest neighbor exchange, resulting in a zigzag spin configuration. As in Ref. 20, we also take into account the presence of both an easy-axis and a hard-axis anisotropy. The hard-axis lies out of the plane, which forces the spins to align in-plane, while the weaker easy-axis anisotropy favors spin alignment along the z-direction in the ground state. Our computed values are in closer agreement with the latest experimental results.[20,21] While the next-next-nearest exchange shows good agreement with the experiments, the calculated nearest and next-nearest neighbor exchanges are far weaker than the observed values. The experiments also observe that the hard-axis is canted at an angle of 73°, while the DFT calculations find the hard-axis to be completely perpendicular to the zx-plane.

TABLE II. Values for exchange and anisotropy constants obtained via neutron scattering experiments[19,20] and calculated in this paper via DFT. The values are given in meV.

Parameter	Ref. 19	Ref. 20	DFT
$\mathcal{J}_1$	1.9	1.3	0.1
$\mathcal{J}_2$	−0.1	−0.1	−0.003
$\mathcal{J}_3$	−6.9	−6.8	−5.7
$\mathcal{J}_\perp$	0.3	0.3	…
$\mathcal{D}_x$	0	0	0
$\mathcal{D}_y$	0	−0.21	−0.003
$\mathcal{D}_z$	0.3	0.01	0.025

The apparent discrepancy in the reported canting angle associated with the hard-axis can be understood by considering the different physical origins of the hard-axis anisotropy. Unlike the easy-axis anisotropy, which originates from lattice distortions induced by spin-lattice coupling in the magnetic ground state, the hard-axis anisotropy arises from the intrinsic structural anisotropy of the $NiPS_3$ lattice, which is inequivalent along the y-direction. As discussed in Sec. II, for a monolayer, there is no shifted stacking. This results in a calculated hard-axis, which is perpendicular to the film. The absence of layers in the out-of-plane direction may also be the reason for the calculated hard-axis anisotropy in the monolayer being much smaller than the observed anisotropy in bulk. This canting of the spins does not result in any qualitative changes and thus can be neglected in the analysis. The significant difference between the theoretical and experimental nearest and next-nearest neighbor exchange constants is not necessarily a problem of the DFT method, but may indicate that calculations for the monolayer are not well suited to model bulk material properties since they underestimate the splitting of the optical and acoustic bands by roughly 30 meV. Unfortunately, our DFT method cannot accurately calculate the weak van der Waals interlayer exchange and, hence, bilayer and bulk materials. We, therefore, adopt exchange and anisotropy constants for the bilayer and bulk samples from prior neutron scattering experiments.[19–21] In Sec. IV, we present the analytical magnon dispersion in $NiPS_3$.

IV. SPIN-WAVE DISPERSION SPECTRA

Here, we solve the linearized LL equation in order to calculate the magnon dispersion in $NiPS_3$ for a monolayer and a bilayer and in the bulk. We focus on the dispersion for the collinear antiferromagnetic phase.

A. Monolayer

In the antiferromagnetic phase [Fig. 3(a)], the spins lie completely in the plane, along the easy-axis. Substituting Eq. (6) in Eq. (4) results in a linear eigenvalue problem.[19,31] Solving the eigenvalue problem results in the full magnon dispersion (see Appendix A). We recover the results from Ref. 19 by disregarding the hard-axis; i.e., $D_y = 0$. In this case, the eigenvalues are

$$\begin{aligned}
\omega_1 &= B_0 - \sqrt{A^2 - |C|^2 - B^2 - |D|^2 + \sqrt{D^*\left(4B(AC+BD) + |C|^2 D^*\right) + C^*\left(4A(AC+BD) - 2C|D|^2\right) + D^2(C^*)^2}},\\
\omega_2 &= B_0 + \sqrt{A^2 - |C|^2 - B^2 - |D|^2 + \sqrt{D^*\left(4B(AC+BD) + |C|^2 D^*\right) + C^*\left(4A(AC+BD) - 2C|D|^2\right) + D^2(C^*)^2}},\\
\omega_3 &= B_0 - \sqrt{A^2 - |C|^2 - B^2 - |D|^2 - \sqrt{D^*\left(4B(AC+BD) + |C|^2 D^*\right) + C^*\left(4A(AC+BD) - 2C|D|^2\right) + D^2(C^*)^2}},\\
\omega_4 &= B_0 + \sqrt{A^2 - |C|^2 - B^2 - |D|^2 - \sqrt{D^*\left(4B(AC+BD) + |C|^2 D^*\right) + C^*\left(4A(AC+BD) - 2C|D|^2\right) + D^2(C^*)^2}}.
\end{aligned} \tag{10}$$

Otherwise, analytical solutions are tedious. However, when $k_x = 0$, the eigenvalue problem is easily solvable again and

$$\begin{aligned}
\omega_{1\pm}^2 &= B_0^2 + (A-C)(A_1-C) - (B+D)^2 \pm \sqrt{B_0^2(A+A_1+2(B-C+D))(A+A_1-2(B+C+D)) + (A-A_1)^2(B+D)^2},\\
\omega_{2\pm}^2 &= B_0^2 + (A+C)(A_1+C) - (B-D)^2 \pm \sqrt{B_0^2(A+A_1+2(B+C-D))(A+A_1+2(C+D-B)) + (A-A_1)^2(B-D)^2},
\end{aligned} \tag{11}$$

where

$$\begin{gathered}
A = 2\left[D_z + J_1 - 2J_2\cos\left(\sqrt{3}k_z l_a\right) - 2J_2 - 3J_3\right], \quad A_1 = 2(A + D_y),\\
B = 8J_2\cos\left(\sqrt{3}k_z l_a/2\right)\cos(3k_x l_a/2),\\
C = 4J_1 e^{-ik_x l_a/2}\cos\left(\sqrt{3}k_z l_a/2\right),\\
D = 2\left[e^{ik_x l_a}\left(J_1 + 2J_3\cos\left(\sqrt{3}k_z l_a\right)\right) + J_3 e^{2ik_x l_a}\right].
\end{gathered} \tag{12}$$

Figure 4 presents the magnon dispersion for monolayer $NiPS_3$ in the absence of anisotropy or external magnetic fields. Among in-plane antiferromagnetic materials, $NiPS_3$ is notable for its exceptionally low anisotropy strength.[16] To establish a baseline, we first analyze the key features of the dispersion in the isotropic limit, before incorporating anisotropy into the system. The exchange constants are taken from Ref. 20 and shown in Table II. Figure 4(a) shows two-dimensional cutouts along high-symmetry paths in the Brillouin zone, while the full dispersion across the reciprocal space is depicted in Fig. 4(b). The results in Fig. 4 reveal that, in the absence of an external field, the four frequency bands originating from the four sublattices appear as two doubly degenerate bands. The bands form in pairs of higher and lower-energy bands. In the higher bands, the up and down spins precess out-of-phase with each other, forming the optical modes. In the lower bands, the up- and down-spin precess in-phase with each other. The optical and acoustic magnon modes are analogous to the antibonding and bonding orbitals formed in the hydrogen molecule by the destructive and constructive interference of the atomic orbitals, respectively. Additionally, we observe Dirac cones as in other antiferromagnetic materials on a hexagonal lattice. A striking feature of the dispersion is the quadruply degenerate line of linear crossings along the Z–C direction forming a Dirac nodal line [see Fig. 4(c)] as predicted for hexagonal zigzag antiferromagnetic systems.[23,28]

In Fig. 5, we present the magnon dispersion, incorporating both anisotropy and an external magnetic field using exchange and anisotropy constants from neutron scattering experiments[20] [Figs. 5(a)–5(b)], and those obtained via first-principles calculations [Figs. 5(c)–5(d)]. Figure 5(a) shows the dispersion in the absence of an external field. The degeneracy of the Dirac cones is lifted by the anisotropy. Furthermore, even without an external field, the bands exhibit a small splitting around the points Γ and C due to the hard-axis anisotropy, revealing four distinct bands. The observed splitting of the magnon bands arises directly from the presence of a hard-axis anisotropy and is consistent with Refs. 20 and 21. This splitting is absent in Ref. 19, where a hard-axis term is not included in the Hamiltonian used to compute the magnon spectra. Along the Z–C direction, the quadruply degenerate Dirac nodal line is split into two doubly degenerate Dirac nodal lines (although the splitting due to the hard-axis is very small).

In Fig. 5(b), we plot the dispersion with anisotropies and a weak external field ($B_0 < B_c$) applied along the easy-axis. The external field leads to additional splittings or increases the ones induced by the anisotropy. However, along the Z–C direction, the two Dirac nodal lines remain doubly degenerate. This persistence suggests that the two doubly degenerate Dirac nodal lines between Z and C are robust against both anisotropy and the external magnetic field. Dirac nodal lines in zigzag antiferromagnets possess topological protection due to a combination of nonsymmorphic and time-reversal symmetries.[23,28,29]

The dispersion calculated and published in Refs. 20 and 21 considers a 73.02° spin canting from the hard-axis. We have to adopt a perpendicular magnetization to analytically solve the LL equation. Nevertheless, our results for the magnon dispersion do not differ much from those in Refs. 20 and 21.

Next, we plot the magnon dispersion using the exchange and anisotropy constants for the monolayer from first-principles calculations in Fig. 5(c) using the DFT-derived parameters listed in Table II. The overall features closely resemble those in Fig. 5(a): the degeneracy is lifted at the high-symmetry points, and Dirac nodal lines appear along the Z–C direction. The main distinction is the energy gap between the optical and acoustic branches at the Γ point. In the DFT, this gap of 30 meV is too small compared with the experiment. This

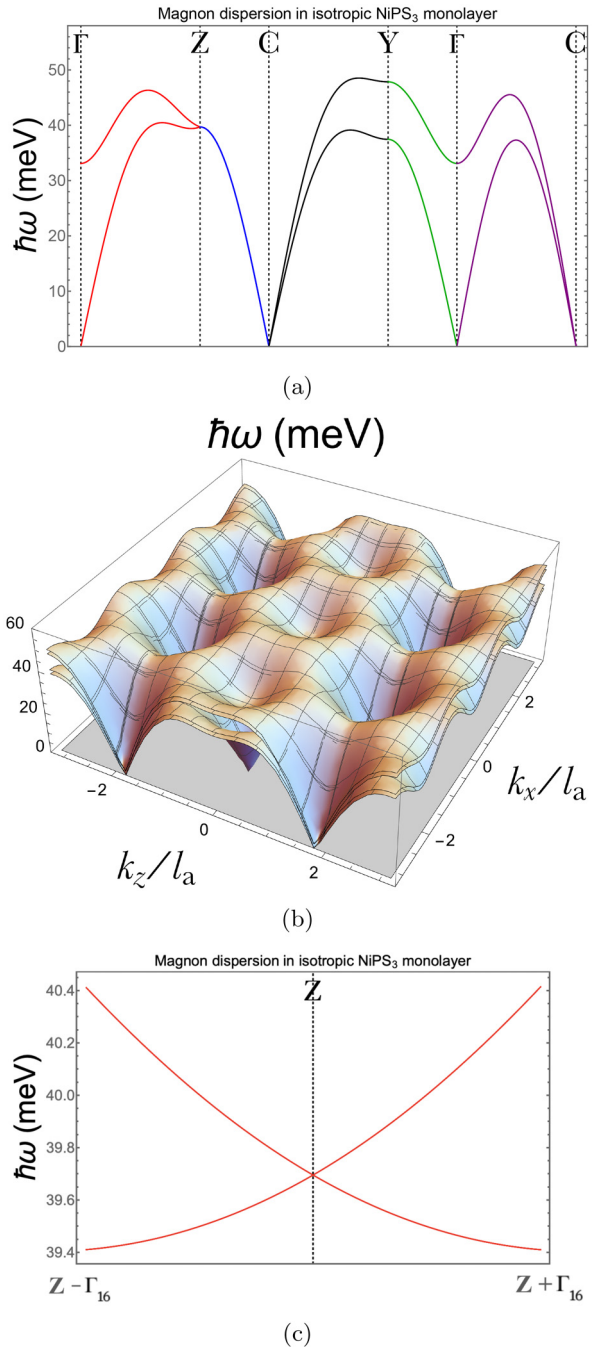

FIG. 4. Spin-wave dispersion in a monolayer $NiPS_3$ in the absence of anisotropy with only the exchange interactions considered. (a) Line cuts of the dispersion along the relevant paths in the Brillouin zone, also marked in Fig. 1(b). (b) 2D dispersion in the reciprocal space. The values for exchange interactions are taken from Ref. 20 and shown in Table II. (c) Dispersion around the Z point revealing a linear magnon band crossing. The point at the crossing remains degenerate throughout Z–C, forming a Dirac nodal line. Γ_{16} is 1/16th the distance between Γ and Z along k_z.

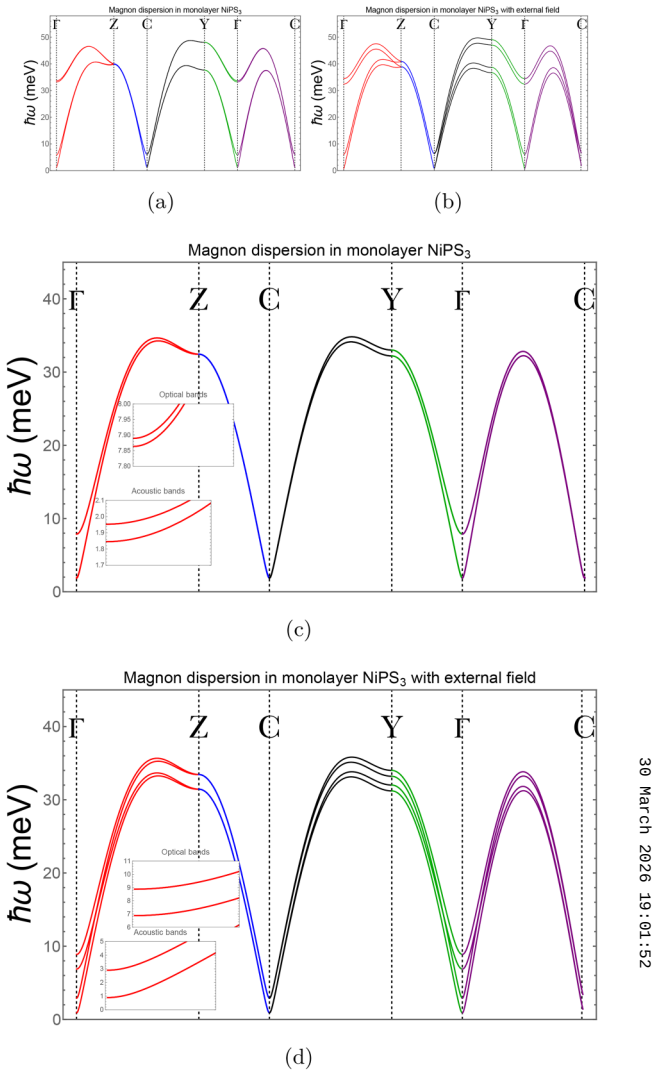

FIG. 5. Spin-wave dispersion of monolayer $NiPS_3$ under different field conditions and exchange and anisotropy constants. (a) Dispersion calculated for a monolayer including both easy-axis and hard-axis anisotropy in the absence of an external magnetic field, using exchange and anisotropy constants obtained from Ref. 20. (b) Corresponding dispersion for the same parameters in the presence of a 2 T (0.25 meV) magnetic field applied along the easy-axis. (c) Dispersion computed using the exchange and anisotropy constants calculated using DFT for zero applied field. (d) Dispersion for the same parameter set under a 2 T field applied along the easy-axis. The hard-axis is taken perpendicular to the plane, resulting in an in-plane equilibrium spin orientation. Insets show magnified regions near the Γ point highlighting the optical (upper) and acoustic (lower) branches. The exchange and anisotropy constants are shown in Table II.

difference arises primarily from underestimated exchange interactions between nearest and next-nearest neighbors. We study the effect of an external field on the dispersion with DFT-derived values in Fig. 5(d). The bands split as expected, but the splitting is smaller than that calculated with experimental parameters adopted from Ref. 20.

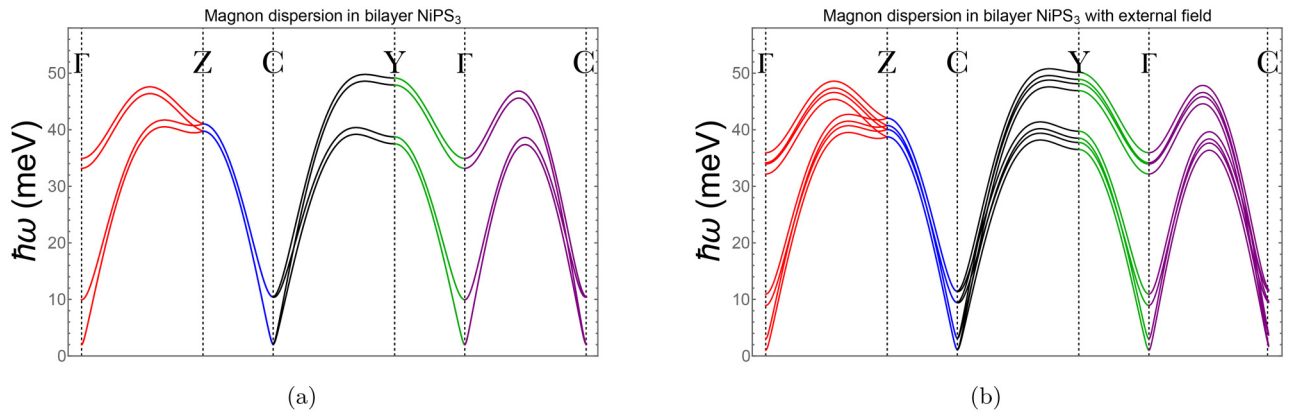

FIG. 6. Magnon dispersion in a bilayer $NiPS_3$ in (a) the absence of an externally applied magnetic field and (b) in the presence of an externally applied magnetic field of 2 T (0.25 meV) applied along the easy-axis. The exchange and anisotropy constants are taken from Ref. 20 and shown in Table II.

In neutron scattering measurements of magnetic excitations, lattice vibrations can contribute to the inelastic signal and must be carefully distinguished from magnetic scattering. Lançon *et al.*[19] explicitly account for phonon contributions by exploiting the contrasting momentum-transfer dependence of magnetic and lattice scattering to estimate and subtract the phonon background. In contrast, Wildes *et al.*[20] focus on low-energy magnetic excitations, where the magnon signal is dominant and well separated from phonon modes, allowing the data to be consistently interpreted without an explicit treatment of phonon scattering. Motivated by these approaches, we discuss the role of phonons in $NiPS_3$ and the implications for interpreting magnon dispersions in Appendix F.

In Subsection IV B, we calculate and plot the dispersion for bilayer $NiPS_3$. Since our first principles methods do not show significant agreement for bilayer and bulk systems, we use the values from Ref. 20 for all further results shown in this paper.

B. Bilayer

The bilayer $NiPS_3$[16,20,21,25,31] can be thought of as two ferromagnetically coupled antiferromagnetic monolayers with spin Hamiltonian:[16,20]

$$\hat{H}_{bil} = \hat{H}^1{}_{mono} + \hat{H}^2{}_{mono} - \sum_{j,\sigma_\perp} \mathcal{J}_\perp \overrightarrow{S}_j \cdot \overrightarrow{S}_{j+\sigma_\perp}, \tag{13}$$

where H^i_{mono} is the Hamiltonian for layer $i \in (1, 2)$, $\mathcal{J}_\perp > 0$ is the interlayer exchange, $\overrightarrow{S}_j$ is the spin at lattice site j, and $\overrightarrow{S}_{j+\sigma_\perp}$ denotes the spin at the lattice site directly above or below site j. The Landau–Lifshitz (LL) equation for the bilayer becomes a 16×16 matrix equation that we solve numerically. We show the derivation of this matrix in Appendix B. Figure 6 presents the dispersion for bilayer $NiPS_3$ along high-symmetry paths in the Brillouin zone. The number of independent sublattices and spin bands is 8.

In Fig. 6(a), we show the dispersion for the bilayer in the absence of an external magnetic field. As in the monolayer, the bands split at lower values of k and become nearly degenerate at higher k. The bilayer exhibits four doubly degenerate Dirac nodal lines. The interlayer exchange interaction introduces new crossings near C, similar to the crossings seen in the monolayer under an applied external field.

In Fig. 6(b), we present the dispersion for bilayer $NiPS_3$ in the presence of a magnetic field applied along the easy-axis ($B_0 < B_c$) that results in the splitting of spin-degenerate bands. The Dirac nodal lines between Z and C remain doubly degenerate. We also observe additional crossings emerging near C upon the application of the external field. The dispersion in bulk $NiPS_3$[20,21] can be calculated similarly by replacing A with $A_b = A + 2J_\perp(1 - \cos\sqrt{3}k_y l_b)$ in Eq. (12). We treat the bulk in greater detail in Appendix C.

In Sec. V, we compute the evolution of the resonance frequency when the external magnetic field is strong enough to reorient the ground states.

V. ANTIFERROMAGNETIC RESONANCE FREQUENCY

Here, we compute the antiferromagnetic resonance (AFMR) frequencies,[16,31] i.e., the frequencies of the eigenmodes at $k = 0$ as a function of an external magnetic field applied in-plane both along and perpendicular to the easy-axis.

A. Monolayer

For $B_0 < B_c$ along the Néel vector, the spins in the monolayer ground state stay in the collinear antiferromagnetic ground state. When $B_0 > B_c$, the spins transit into the "spin-flop" phase, as described in Sec. II [see Fig. 3(b)]. The resonance frequencies in this regime are given by (see Appendix D)

$$\begin{aligned}
\omega^{sf}_{1\pm} &= \pm\sqrt{(B_{sf0} + A_{sf} - B_{sf1} - C_{sf} - D_{sf1})(B_{sf} + A_{sf1} - B_{sf} - C_{sf} - D_{sf})},\\
\omega^{sf}_{2\pm} &= \pm\sqrt{(B_{sf0} + A_{sf} + B_{sf1} + C_{sf} - D_{sf1})(B_{sf} + A_{sf1} + B_{sf} + C_{sf} - D_{sf})},\\
\omega^{sf}_{3\pm} &= \pm\sqrt{(B_{sf0} + A_{sf} + B_{sf1} - C_{sf} + D_{sf1})(B_{sf} + A_{sf1} + B_{sf} - C_{sf} + D_{sf})},\\
\omega^{sf}_{4\pm} &= \pm\sqrt{(B_{sf0} + A_{sf} - B_{sf1} + C_{sf} + D_{sf1})(B_{sf} + A_{sf1} - B_{sf} + C_{sf} + D_{sf})},
\end{aligned} \tag{14}$$

where

$$
\begin{aligned}
B_{sf0} &= B_0 \sin\theta_{sf},\\
A_{sf} &= 2\big(D_z \sin^2\theta_{sf} + (2-\cos 2\theta_{sf})J_1\\
&\quad -(4\cos 2\theta_{sf}-2)J_2 \cos\left(\sqrt{3}k_z l_a\right) - 3J_3 \cos 2\theta_{sf}\big),\\
A_{sf1} &= A_{sf} + 2D_y,\\
B_{sf} &= 2\left[J_2 \cos\left(\sqrt{3}k_z l_a\right)\cos(3k_x l_a/2)\right],\\
B_{sf1} &= 4B\cos 2\theta_{sf},\\
C_{sf} &= 4J_1 e^{-ik_x l_a/2}\cos\left(\sqrt{3}k_z l_a\right),\\
D_{sf} &= 2\left[e^{ik_x l_a}\left(J_1 + 2J_3\cos\left(\sqrt{3}k_z l_a\right)\right) + J_3 e^{2ik_x l_a}\right],\\
D_{sf1} &= D_{sf}\cos 2\theta_{sf}.
\end{aligned}
\tag{15}
$$

Here, $\sin\theta_{sf}$ is given in Eq. (8).

In Fig. 7(a), we plot the resonance frequency of monolayer $NiPS_3$ as a function of the external magnetic field along the easy-axis using the exchange and anisotropy constants given in Ref. 20. The external magnetic field again Zeeman-splits the spin degeneracies. At B_c, the lower band becomes soft, signaling the transition from the antiferromagnetic phase to the spin-flop phase. We calculate $B_c \approx 15$ T, which is close to the experimental value of 10 T[27] in the bulk. The resonance frequency in the monolayer as a function of magnetic field has not been studied experimentally to the best of our knowledge. The higher bands show a discontinuous jump at B_c as expected.[31] Upon increasing the magnetic field to $B_{sat} = 2(D_x - D_z - J_{af})$, the lowest frequency band once again vanishes and all the spins align along the magnetic field direction (ferromagnetic phase, see Fig. 11 for the AFMR frequency across the full range of B_0). Upon increasing the magnetic field further, the bands cross at multiple points. The expression for the resonance frequency in the canted state closely resembles that of the spin-flop state. Substituting θ_{sf} in Eq. (8) with θ_c from Eq. (9) and replacing $\sin^2(\theta_{sf})D_z$ with $\cos^2(\theta_c)D_z$ yields the resonance frequency for the canted state. In Fig. 7(b), we show the resonance frequency as a function of an in-plane magnetic field applied perpendicular to the easy-axis. Under this configuration, the spins immediately transition to the canted state with an angle θ_c determined by Eq. (9). In the canted state, only the lowest mode changes significantly for a magnetic field of up to 30 T. At the saturation field, the lowest frequency again goes to zero (see Fig. 11).

B. Bilayer

Finally, we examine the resonance frequency in the bilayer system. In Fig. 8, we plot its resonance frequency as a function of an external magnetic field applied in-plane, along the easy-axis, or perpendicular to the easy-axis. The interlayer exchange interaction between the two layer splits the frequency into eight distinct bands. The overall behavior is similar to that of the monolayer. Figure 8(a) presents the resonance frequency for bilayer $NiPS_3$ under an external field applied along the easy-axis. The bands are Zeeman-split by the magnetic field. At $B = B_c$, the lowest frequency band becomes soft at the spin-flop transition. Additionally, a new crossing of the resonance frequency bands is visible in the bilayer below B_c.

In Fig. 8(b), we show the resonance frequency under an external magnetic field applied perpendicular to the easy-axis. In this case, the spins immediately develop a finite canting angle that increases with the magnetic field. Similar to the monolayer, only the lowest mode changes significantly for $B_0 < 30$ T in the canted state.

Spin currents injected into non-collinear antiferromagnets (such as $NiPS_3$ in the spin-flop state) with a fixed polarization excite linear combinations of the magnon eigenstates that, therefore, lead to coherent oscillations in the magnet. This magnon Hanle effect[45–47] is prominent in the proximity of magnon band degeneracies. In both the spin-flop and canted states, the application of a magnetic field ($B_0 > B_c$) generates numerous additional crossings between the magnon branches (see Fig. 11). These crossings extend beyond the AFMR frequency to points throughout the Brillouin zone (see Fig. 12 in Appendix D). These degeneracies at non-zero group velocities in the bilayer fulfill the requirements of the magnon Hanle effect. As in the monolayer, the lowest magnon branch softens as the field approaches the saturation value, as illustrated in Fig. 11.

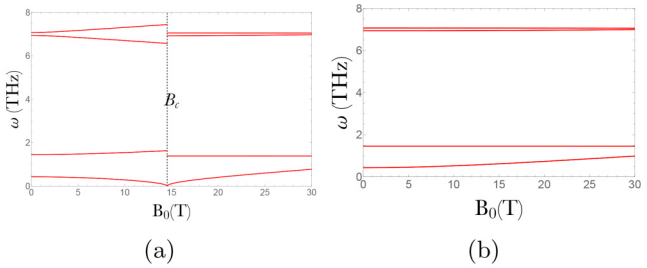

FIG. 7. AFMR frequency in monolayer $NiPS_3$ vs (a) external in-plane magnetic field B_0 applied along the easy-axis and (b) external in-plane magnetic field B_0 applied along the intermediate axis. The exchange and anisotropy constants are taken from Ref. 20 and shown in Table II.

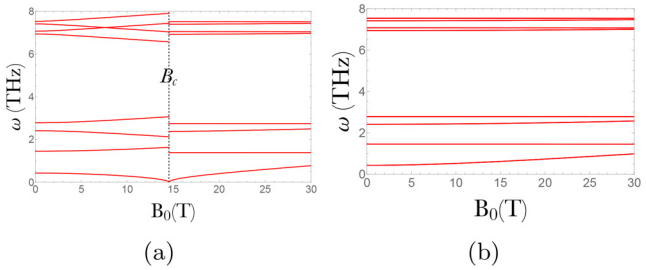

FIG. 8. AFMR frequency of bilayer $NiPS_3$ as a function of (a) external in-plane magnetic field B_0 along the easy-axis and (b) in-plane magnetic field B_0 applied along the intermediate axis. The exchange and anisotropy constants are taken from Ref. 20 and shown in Table II.

VI. CONCLUSION

We developed a computational framework for the magnon dispersion and resonance behavior of monolayer and bilayer van der Waals magnet $NiPS_3$ based on the Landau–Lifshitz equation using exchange and anisotropy parameters obtained from both first-principles calculations and neutron scattering experiments. For the monolayer, first-principles methods confirm a zigzag antiferromagnetic ground state and reproduce the features of the magnon spectrum, including the presence of Dirac nodal lines that persist under applied magnetic fields and anisotropy. However, the DFT-derived exchange parameters underestimate the splitting of the optical and acoustic magnon modes at the Γ point by 30 meV, reflecting the limitations of first-principles approaches in describing interlayer and long-range exchange interactions. For bilayer and bulk $NiPS_3$, we adopt experimentally extracted exchange parameters.

Our findings are in good agreement with previously reported experimental results but do not explain the observed tilting of the hard-axis from the surface normal. The presence of a hard-axis induces weak band splitting at the Γ and C points, a signature of the hard-axis that has been observed in neutron scattering experiments.[20,21] In the bilayer system, interlayer exchange splits the bands while preserving the degenerate Dirac lines. Furthermore, we investigate the antiferromagnetic resonance (AFMR) frequency as a function of the external magnetic field applied both parallel and perpendicular to the easy-axis, noting significant differences in the behavior of the system across antiferromagnetic, spin-flop, and ferromagnetic states. We find a spin-flop field of around 15 T using experimentally extracted parameters. We briefly discuss bulk $NiPS_3$ and relegate the details of the bulk to Appendix C.

Our work provides analytical expressions for the AFMR frequency as a function of the magnetic field for both monolayer and bilayer $NiPS_3$. Throughout this study, we assume that the hard-axis is perpendicular to the crystallographic plane, resulting in spins that are fully confined to the plane in the ground state. This assumption allows for analytical solutions for the dispersion and resonance frequency. Experiments indicate a magnetic structure in which the hard-axis is slightly canted with an angle of 73° with the plane. However, the DFT calculations could not reproduce these results. This symmetry breaking would significantly complicate the spin model calculations without much changing the results.

ACKNOWLEDGMENTS

This publication is part of the project "Ronde Open Competitie ENW pakket 21-3" (File No. OCENW.M.21.215) and "Ronde Open Competitie XL" (File No. OCENW.XL21.058), which are (partly) financed by the Dutch Research Council (NWO). A.V.B. was supported by EUProject No. HORIZON-EIC-2021-PATHFINDEROPEN-01 PALANTIRI-101046630. J.F. has been funded by project PID2022-137078NB-I00 (MCIN/AEI/10.13039/501100011033/FEDER, EU) and the Horizon Europe project TRILMAX (Grant No. 101159646). E.V.T. was supported by the National Science Center of Poland (Project No. UMO-2023/49/B/ST3/02920). G.E.W.B. was supported by JSPS Kakenhi (Grant Nos. 22H04965 and JP24H02231).

AUTHOR DECLARATIONS

Conflict of Interest

The authors have no conflicts to disclose.

Author Contributions

Ritesh Das: Formal analysis (equal); Visualization (equal); Writing – original draft (equal). **Rob den Teuling:** Formal analysis (supporting); Validation (supporting); Visualization (supporting); Writing – review & editing (supporting). **Artem V. Bondarenko:** Formal analysis (supporting); Validation (supporting); Visualization (supporting); Writing – review & editing (supporting). **Elena V. Tartakovskaya:** Formal analysis (supporting); Supervision (supporting); Writing – review & editing (supporting). **Gerrit E. W. Bauer:** Conceptualization (supporting); Supervision (supporting); Writing – review & editing (supporting). **Jaime Ferrer:** Conceptualization (supporting); Formal analysis (supporting); Writing – review & editing (supporting). **Yaroslav M. Blanter:** Conceptualization (equal); Supervision (equal); Validation (equal); Writing – review & editing (equal).

DATA AVAILABILITY

The data that support the findings of this study are openly available in Zenodo at https://doi.org/10.5281/zenodo.17532238 (Ref. 48) and at https://doi.org/10.5281/zenodo.17529866 (Ref. 49).

APPENDIX A: EIGENVALUE PROBLEM FOR A MONOLAYER

The unit cell in Fig. 1 contains four independent spins. The eigenvalue problem can be written in the basis:

$$\vec{m}_{AF} = \left(m^y_{1a} \quad m^y_{2a} \quad m^y_{1b} \quad m^y_{2b} \quad im^z_{1a} \quad im^z_{2a} \quad im^z_{1b} \quad im^z_{2b}\right)^T. \tag{A1}$$

The sublattices used in the basis are shown in Fig. 1(b). The eigenvalue matrix relating the frequency to the magnetization vector is given by[19]

$$\omega \begin{pmatrix} m^x_{1a} \\ m^x_{2a} \\ m^x_{1b} \\ m^x_{2b} \\ im^y_{1a} \\ im^y_{2a} \\ im^y_{1b} \\ im^y_{2b} \end{pmatrix} = \begin{pmatrix} 0 & 0 & 0 & 0 & B_0 + A_1 & -B & -C & -D \\ 0 & 0 & 0 & 0 & B & B_0 - A_1 & D & C \\ 0 & 0 & 0 & 0 & -C^* & -D^* & B_0 + A_1 & -B \\ 0 & 0 & 0 & 0 & D^* & C^* & B & B_0 - A_1 \\ B_0 + A & -B & -C & -D & 0 & 0 & 0 & 0 \\ B & B_0 - A & D & C & 0 & 0 & 0 & 0 \\ -C^* & -D^* & B_0 + A & -B & 0 & 0 & 0 & 0 \\ D^* & C^* & B & B_0 - A & 0 & 0 & 0 & 0 \end{pmatrix} \begin{pmatrix} m^x_{1a} \\ m^x_{2a} \\ m^x_{1b} \\ m^x_{2b} \\ im^y_{1a} \\ im^y_{2a} \\ im^y_{1b} \\ im^y_{2b} \end{pmatrix}. \tag{A2}$$

APPENDIX B: EIGENVALUE PROBLEM FOR A BILAYER

The magnetic structure for the primitive unit cell for bilayer $NiPS_3$ is shown in Fig. 1(a). The bilayer is described by a unit cell with eight sublattices, four for each layer. For eight sublattices, the resulting eigenvalue problem is given as

$$\omega^b \begin{pmatrix} m^x_{1au} \\ m^x_{2au} \\ m^x_{1bu} \\ m^x_{2bu} \\ m^x_{1ad} \\ m^x_{2ad} \\ m^x_{1bd} \\ m^x_{2bd} \\ im^y_{1au} \\ im^y_{2au} \\ im^y_{1bu} \\ im^y_{2bu} \\ im^y_{1ad} \\ im^y_{2ad} \\ im^y_{1bd} \\ im^y_{2bd} \end{pmatrix} = \begin{pmatrix} 0 & 0 & 0 & 0 & 0 & 0 & 0 & 0 & B_0+A_{1b} & -B & -C & -D & -J_\perp & 0 & 0 & 0 \\ 0 & 0 & 0 & 0 & 0 & 0 & 0 & 0 & B & B_0-A_{1b} & D & C & 0 & J_\perp & 0 & 0 \\ 0 & 0 & 0 & 0 & 0 & 0 & 0 & 0 & -C^* & -D^* & B_0+A_{1b} & -B & 0 & 0 & -J_\perp & 0 \\ 0 & 0 & 0 & 0 & 0 & 0 & 0 & 0 & D^* & C^* & B & B_0-A_{1b} & 0 & 0 & 0 & J_\perp \\ 0 & 0 & 0 & 0 & 0 & 0 & 0 & 0 & -J_\perp & 0 & 0 & 0 & B_0+A_{1b} & -B & -C & -D \\ 0 & 0 & 0 & 0 & 0 & 0 & 0 & 0 & 0 & J_\perp & 0 & 0 & B & B_0-A_{1b} & D & C \\ 0 & 0 & 0 & 0 & 0 & 0 & 0 & 0 & 0 & 0 & -J_\perp & 0 & -C^* & -D^* & B_0+A_{1b} & -B \\ 0 & 0 & 0 & 0 & 0 & 0 & 0 & 0 & 0 & 0 & 0 & J_\perp & D^* & C^* & B & B_0-A_{1b} \\ B_0+A_b & -B & -C & -D & -J_\perp & 0 & 0 & 0 & 0 & 0 & 0 & 0 & 0 & 0 & 0 & 0 \\ B & B_0-A_b & D & C & 0 & J_\perp & 0 & 0 & 0 & 0 & 0 & 0 & 0 & 0 & 0 & 0 \\ -C^* & -D^* & B_0+A_b & -B & 0 & 0 & -J_\perp & 0 & 0 & 0 & 0 & 0 & 0 & 0 & 0 & 0 \\ D^* & C^* & B & B_0-A_b & 0 & 0 & 0 & J_\perp & 0 & 0 & 0 & 0 & 0 & 0 & 0 & 0 \\ -J_\perp & 0 & 0 & 0 & B_0+A_b & -B & -C & -D & 0 & 0 & 0 & 0 & 0 & 0 & 0 & 0 \\ 0 & J_\perp & 0 & 0 & B & B_0-A_b & D & C & 0 & 0 & 0 & 0 & 0 & 0 & 0 & 0 \\ 0 & 0 & J_\perp & 0 & -C^* & -D^* & B_0+A_b & -B & 0 & 0 & 0 & 0 & 0 & 0 & 0 & 0 \\ 0 & 0 & 0 & -J_\perp & D^* & C^* & B & B_0-A_b & 0 & 0 & 0 & 0 & 0 & 0 & 0 & 0 \end{pmatrix} \times \begin{pmatrix} m^x_{1au} \\ m^x_{2au} \\ m^x_{1bu} \\ m^x_{2bu} \\ m^x_{1ad} \\ m^x_{2ad} \\ m^x_{1bd} \\ m^x_{2bd} \\ im^y_{1au} \\ im^y_{2au} \\ im^y_{1bu} \\ im^y_{2bu} \\ im^y_{1ad} \\ im^y_{2ad} \\ im^y_{1bd} \\ im^y_{2bd} \end{pmatrix}, \tag{B1}$$

where $A_{1b} = A_1 + J_\perp$, $A_b = A + J_\perp$, $J_\perp = \frac{\mathcal{J}_k S}{\gamma\hbar}$.

APPENDIX C: BULK

The bulk configuration can be described using the same unit as the monolayer. Thus, the unit cell has four sublattices. The unit cell can be repeated over all directions to span the entire structure. Figure 9 shows the magnon dispersion for bulk $NiPS_3$ over the Brillouin zone in the plane for different k_y. k_y is in units of $1/c$, where c is the lattice constant in the y direction. In Fig. 9(a), we plot the dispersion for bulk $NiPS_3$ in the absence of an external magnetic field for different k_y. In Fig. 9(b), we plot the dispersion for bulk $NiPS_3$ in the presence of an external magnetic field for different k_y. Due to small interlayer exchange, the differences with the bilayer are small.

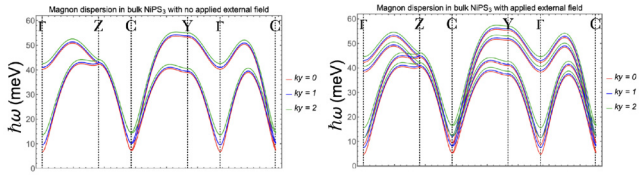

FIG. 9. Magnon dispersion in bulk $NiPS_3$ for different values of k_y in (a) the absence of an externally applied magnetic field and (b) in the presence of an externally applied magnetic field of 2 T (0.25 meV). The exchange constants and anisotropy constants are taken from neutron scattering experiments conducted in Ref. 20. The values are taken from Ref. 20. k_y is in units of l_b.

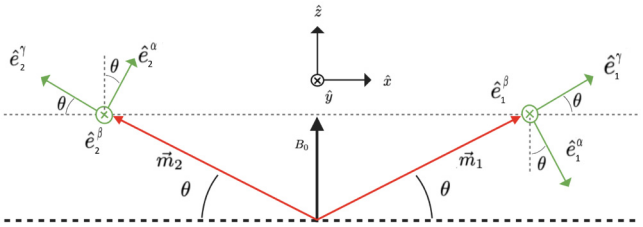

FIG. 10. Spins in sublattice $\vec{m}_1$ and $\vec{m}_2$. The new coordinate systems are shown with respect to the Cartesian basis. Note that $\vec{m}_{1(2)}$ lies exactly along $\hat{e}^{A(B)}_{\gamma}$.

APPENDIX D: SPIN-FLOP/CANTED STATE

In order to describe the excitations of the spin-flop ground state, we define two new coordinate systems such that the component of the spin-up/spin-down magnetization is constant along at least one direction in the new coordinate system. This is a well-known standard procedure for linearizing the LL equation in the case of the spin-flop ground state.[31] Let $(\hat{e}^{\alpha}_{1(2)}, \hat{e}^{\beta}_{1(2)}, \hat{e}^{\gamma}_{1(2)})$ be an orthogonal coordinate system such that the component of spins in the spin-up (spin-down) sublattice, denoted by $\vec{m}_{1(2)}$, is constant along $\hat{e}^{\gamma}_{1(2)}$ (see Fig. 10).

The transformations relating the new coordinate system to the Cartesian system of coordinates are given by

$$\begin{aligned} \vec{x} &= \sin\theta\hat{e}^{\alpha}_1 + \cos\theta\hat{e}^{\gamma}_1 = \sin\theta\hat{e}^{\alpha}_2 - \cos\theta\hat{e}^{\gamma}_2, \\ \vec{y} &= \hat{e}^{\beta}_1 = \hat{e}^{\gamma}_1, \\ \vec{z} &= -\cos\theta\hat{e}^{\alpha}_1 + \sin\theta\hat{e}^{\gamma}_1 = \cos\theta\hat{e}^{\alpha}_2 + \sin\theta\hat{e}^{\gamma}_2. \end{aligned} \tag{D1}$$

In the new basis, we can write the magnetization as

$$\begin{aligned} \vec{m_1} &= m^{\gamma}_1\hat{e}^{\gamma}_1 + \left(m^{\alpha}_1\hat{e}^{\alpha}_1 + m^{\beta}_1\hat{e}^{\beta}_1\right)e^{i(\omega t - k_x x - k_y y - k_z z)}, \\ \vec{m_2} &= m^{\gamma}_2\hat{e}^{\gamma}_2 + \left(m^{\alpha}_2\hat{e}^{\alpha}_2 + m^{\beta}_2\hat{e}^{\beta}_2\right)e^{i(\omega t - k_x x - k_y y - k_z z)}. \end{aligned} \tag{D2}$$

Assuming $m^{\gamma}_A = m^{\gamma}_B = 1$, we can substitute the ansatz [Eq. (D2)] into Eq. (4) to get the eigenvalue problem relating the frequency to the magnetization in the new basis. We use the sublattices shown in Fig. 1 to form the basis for the eigenvalue problem but in the new coordinate system. The eigenvalue problem in the new basis is

$$\omega^{sf}\begin{pmatrix} m^{\alpha}_{1a} \\ m^{\alpha}_{2a} \\ m^{\alpha}_{1b} \\ m^{\alpha}_{2b} \\ m^{\beta}_{1a} \\ m^{\beta}_{2a} \\ m^{\beta}_{1b} \\ m^{\beta}_{2b} \end{pmatrix} = \begin{pmatrix} 0 & 0 & 0 & 0 & B_{sf0}+A_{sf1} & -B_{sf} & -C_{sf} & -D_{sf} \\ 0 & 0 & 0 & 0 & -B_{sf} & B_{sf0}+A_{sf1} & -D_{sf} & -C_{sf} \\ 0 & 0 & 0 & 0 & -C^{*}_{sf} & -D^{*}_{sf} & B_{sf0}+A_{sf1} & -B_{sf} \\ 0 & 0 & 0 & 0 & -D^{*}_{sf} & -C^{*}_{sf} & -B_{sf} & B_{sf0}+A_{sf1} \\ B_{sf0}+A_{sf} & -B_{sf1} & -C_{sf} & -D_{sf1} & 0 & 0 & 0 & 0 \\ -B_{sf1} & B_{sf0}+A_{sf} & -D_{sf1} & -C_{sf} & 0 & 0 & 0 & 0 \\ -C^{*}_{sf} & -D^{*}_{sf1} & B_{sf0}+A_{sf} & -B_{sf1} & 0 & 0 & 0 & 0 \\ -D^{*}_{sf1} & -C^{*}_{sf} & -B_{sf1} & B_{sf0}+A_{sf} & 0 & 0 & 0 & 0 \end{pmatrix}\begin{pmatrix} m^{\alpha}_{1a} \\ m^{\alpha}_{2a} \\ m^{\alpha}_{1b} \\ m^{\alpha}_{2b} \\ m^{\beta}_{1a} \\ m^{\beta}_{2a} \\ m^{\beta}_{1b} \\ m^{\beta}_{2b} \end{pmatrix}. \tag{D3}$$

Diagonalizing Eq. (D3) for $k = 0$ gives the full AFMR frequency. Figure 11 shows the AFMR frequency in a monolayer and bilayer $NiPS_3$ for the full range of the magnetic field. The resonance frequency across the full range of magnetic field up to saturation is shown in Fig. 11. The magnon dispersion around the Γ point for the canted state of bilayer $NiPS_3$ under different magnetic field

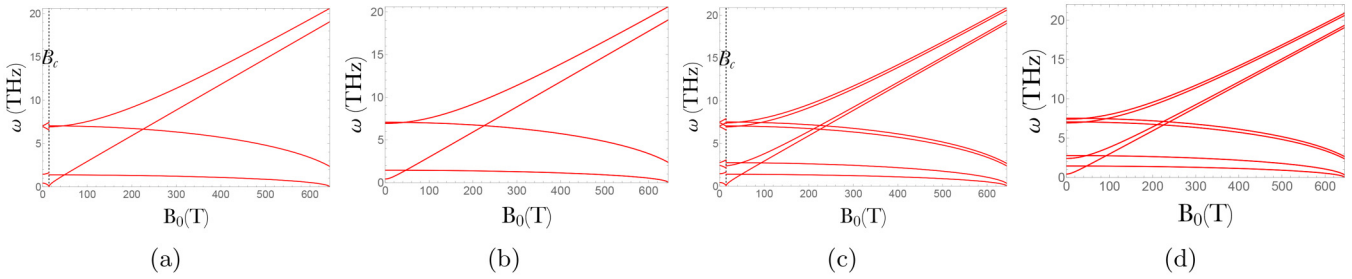

FIG. 11. Full AFMR frequency in (a) monolayer $NiPS_3$ external in-plane magnetic field B_0 applied along the easy-axis and (b) external in-plane magnetic field B_0 applied along the intermediate axis. (c) Full AFMR frequency in bilayer $NiPS_3$ external in-plane magnetic field B_0 applied along the easy-axis and (d) external in-plane magnetic field B_0 applied along the intermediate axis. The exchange and anisotropy constants are taken from Ref. 20. The values are shown in Table II.

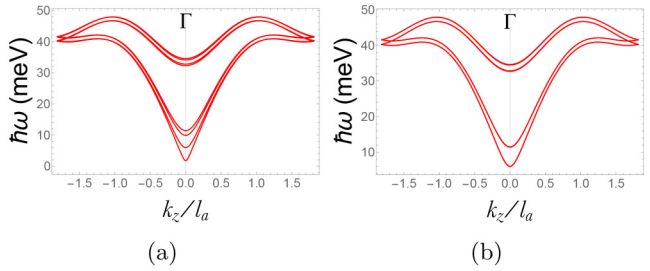

FIG. 12. Magnon dispersion in the canted state around the Γ point for (a) no external field, where the bands are degenerate, and (b) an external field of 49 T, where the bands are degenerate throughout the Brillouin zone.

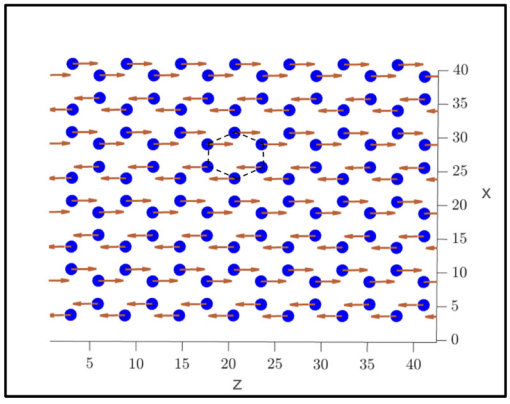

FIG. 13. Monte Carlo simulations with the Metropolis algorithm on a finite $32 \times 24 \times 1$ lattice of $NiPS_3$ at 0.1 K confirming zigzag ordering for DFT-derived exchange and anisotropy constants. The dashed lines show a hexagonal unit cell.

strengths is presented in Fig. 12. Figure 12(a) shows the dispersion in the absence of an external field, where the magnon branches are nondegenerate. In contrast, Fig. 12(b) displays the dispersion at an applied field of 49 T, where the modes become canted and remain degenerate throughout the Brillouin zone. This degeneracy at finite group velocities satisfies the condition required for the magnon Hanle effect.

APPENDIX E: MONTE CARLO SIMULATIONS

Figure 13 presents the outcome of Monte Carlo simulations performed with the Metropolis algorithm on a finite $32 \times 24 \times 1$ lattice of $NiPS_3$ at 0.1 K, confirming the emergence of zigzag antiferromagnetic order. The Metropolis algorithm[37] samples spin configurations by probabilistically accepting or rejecting updates based on energy changes, favoring lower-energy states at low temperatures. This allows the system to efficiently explore the configuration space and settle into its ground state. The dashed lines mark a representative hexagonal unit cell.

APPENDIX F: PHONON DISPERSION AND MAGNON–PHONON COUPLING

In this Appendix, we present the phonon dispersion of $NiPS_3$ obtained from first-principles calculations and discuss the implications for the magnon–phonon coupling. Figure 14 shows the phonon dispersion of monolayer $NiPS_3$ along high-symmetry directions of the Brillouin zone. The acoustic phonon branches are confined to low energies and exhibit relatively weak dispersion, while a dense set of optical phonon modes appears at higher energies.

A key feature of the spectrum is the behavior of the low-energy acoustic modes in relation to the magnon excitations discussed in the main text. The acoustic magnon bands in $NiPS_3$ are relatively steep at low energies, which strongly restricts the available phase space for linear resonant magnon–phonon interactions. Even when the acoustic magnon and phonon dispersions overlap, the

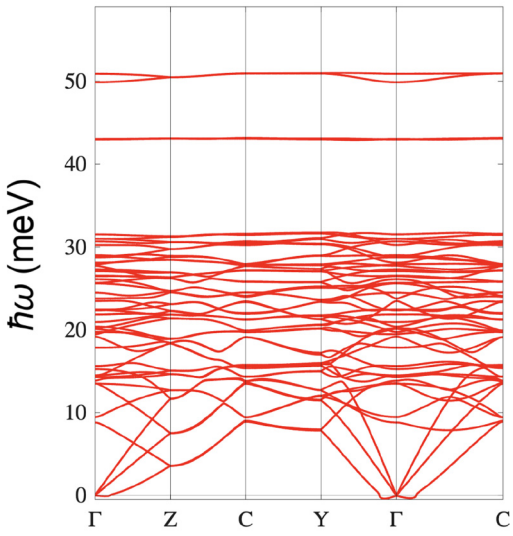

FIG. 14. Phonon modes in monolayer $NiPS_3$ calculated using first-principles methods.

effective coupling in this regime is expected to remain weak due to the small magnon and phonon densities of states and the correspondingly small interaction matrix elements, as shown in the case of Yttrium Iron Garnet (YIG) by Streib *et al.*[50] As a result, the low-energy magnon dispersion is not expected to be significantly affected by lattice dynamics in equilibrium measurements, consistent with experimental observations.[51]

At higher energies, optical phonon branches can, in principle, approach or overlap with magnon bands. In such cases, magnon–phonon coupling may become relevant when allowed by symmetry, as demonstrated in non-collinear antiferromagnets,[52] zigzag antiferromagnets,[53] and layered antiferromagnets.[54] In addition, resonant nonlinear processes involving the emission or absorption of an acoustic phonon by a magnon are, in principle, possible at very small wave vectors through a velocity-matching condition between magnon and phonon modes. However, the phase space available for such processes is extremely limited, and their contribution to the low-energy magnon dispersion is, therefore, expected to be negligible. More generally, non-resonant phonon-mediated interactions between magnons that conserve both energy and momentum are also expected to have a weak effect due to the large separation of characteristic energy scales.[55,56] Further, the experimental realization and detection of higher-order processes of this type typically require strong external excitation or driving of the relevant modes to enhance otherwise weak coupling effects.[55,56] A quantitative analysis of magnon–phonon coupling in this higher-energy regime would require an explicit treatment of dynamical spin–lattice interactions and lies beyond the scope of the present work.

REFERENCES

[1]A. V. Chumak, V. I. Vasyuchka, A. A. Serga, and B. Hillebrands, Nat. Phys. **11**, 453 (2015).
[2]S. M. Rezende, *Fundamentals of Magnonics* (Springer International Publishing, 2020), p. 287.
[3]A. Prabhakar and D. D. Stancil, *Spin Waves: Theory and Applications* (Springer, 2009), Vol. 5.
[4]G. Baghdasaryan and Z. Danoyan, *Magnetoelastic Waves* (Springer, 2017).
[5]A. V. Chumak, P. Kabos, M. Wu, C. Abert, C. Adelmann, A. Adeyeye, J. Åkerman, F. G. Aliev, A. Anane, A. Awad *et al.*, IEEE Trans. Magn. **58**, 1 (2022).
[6]M. Balynsky, D. Gutierrez, H. Chiang, A. Kozhevnikov, G. Dudko, Y. Filimonov, A. Balandin, and A. Khitun, Sci. Rep. **7**, 11539 (2017).
[7]M. Balinskiy, H. Chiang, A. Kozhevnikov, Y. Filimonov, A. Balandin, and A. Khitun, J. Magn. Magn. Mater. **514**, 167046 (2020).
[8]G. E. W. Bauer, E. Saitoh, and B. J. van Wees, Nat. Mater. **11**, 391 (2012).
[9]H. Yu, S. D. Brechet, and J. Ansermet, Phys. Lett. A **381**, 825 (2017).
[10]K. Uchida, Proc. Jpn. Acad. Ser. B **97**, 69 (2021).
[11]A. Mahmoud, F. Ciubotaru, F. Vanderveken, A. V. Chumak, S. Hamdioui, C. Adelmann, and S. Cotofana, J. Appl. Phys. **128**, 161101 (2020).
[12]K. S. Burch, D. Mandrus, and J.-G. Park, Nature **563**, 47 (2018).
[13]M. Blei, J. Lado, Q. Song, D. Dey, O. Erten, V. Pardo, R. Comin, S. Tongay, and A. Botana, Appl. Phys. Rev. **8**, 021301 (2021).
[14]S. Yang, T. Zhang, and C. Jiang, Adv. Sci. **8**, 2002488 (2021).
[15]S. Rahman, J. F. Torres, A. R. Khan, and Y. Lu, ACS Nano **15**, 17175 (2021).
[16]K. Kim, S. Y. Lim, J.-U. Lee, S. Lee, T. Y. Kim, K. Park, G. S. Jeon, C.-H. Park, J.-G. Park, and H. Cheong, Nat. Commun. **10**, 345 (2019).
[17]P. Liu, Y. Zhang, K. Li, Y. Li, and Y. Pu, Science **26**(9), 107584 (2023).
[18]A. R. Wildes, V. Simonet, E. Ressouche, G. J. Mcintyre, M. Avdeev, E. Suard, S. A. Kimber, D. Lançon, G. Pepe, B. Moubaraki *et al.*, Phys. Rev. B **92**, 224408 (2015).
[19]D. Lançon, R. A. Ewings, T. Guidi, F. Formisano, and A. R. Wildes, Phys. Rev. B **98**, 134414 (2018).
[20]A. R. Wildes, J. R. Stewart, M. D. Le, R. A. Ewings, K. C. Rule, G. Deng, and K. Anand, Phys. Rev. B **106**, 174422 (2022).
[21]A. Scheie, P. Park, J. W. Villanova, G. E. Granroth, C. L. Sarkis, H. Zhang, M. B. Stone, J.-G. Park, S. Okamoto, T. Berlijn, and D. A. Tennant, Phys. Rev. B **108**, 104402 (2023).
[22]X. Wang, J. Cao, Z. Lu, A. Cohen, H. Kitadai, T. Li, Q. Tan, M. Wilson, C. H. Lui, D. Smirnov *et al.*, Nat. Mater. **20**, 964 (2021).
[23]K. H. Lee, S. B. Chung, K. Park, and J.-G. Park, Phys. Rev. B **97**, 180401 (2018).
[24]N. D. Mermin and H. Wagner, Phys. Rev. Lett. **17**, 1133 (1966).
[25]K. Mehlawat, A. Alfonsov, S. Selter, Y. Shemerliuk, S. Aswartham, B. Büchner, and V. Kataev, Phys. Rev. B **105**, 214427 (2022).
[26]W. Na, P. Park, S. Oh, J. Kim, A. Scheie, D. A. Tennant, H. C. Lee, J.-G. Park, and H. Cheong, ACS Nano **18**, 20482 (2024).
[27]D. Afanasiev, J. R. Hortensius, M. Matthiesen, S. Mañas-Valero, M. Šiškins, M. Lee, E. Lesne, H. S. van Der Zant, P. G. Steeneken, B. A. Ivanov *et al.*, Sci. Adv. **7**, eabf3096 (2021).
[28]B. Gao, T. Chen, C. Wang, L. Chen, R. Zhong, D. L. Abernathy, D. Xiao, and P. Dai, Phys. Rev. B **104**, 214432 (2021).
[29]K. Li, C. Li, J. Hu, Y. Li, and C. Fang, Phys. Rev. Lett. **119**, 247202 (2017).
[30]L. Landau and E. Lifshitz, *Perspectives in Theoretical Physics* (Elsevier, 1992), pp. 51–65.
[31]S. M. Rezende, A. Azevedo, and R. L. Rodríguez-Suárez, J. Appl. Phys. **126**, 151101 (2019).
[32]J. M. Soler, E. Artacho, J. D. Gale, A. García, J. Junquera, P. Ordejón, and D. Sánchez-Portal, J. Phys.: Condens. Matter **14**, 2745 (2002).
[33]J. P. Perdew, K. Burke, and M. Ernzerhof, Phys. Rev. Lett. **77**, 3865 (1996).
[34]R. Cuadrado, R. Robles, A. García, M. Pruneda, P. Ordejón, J. Ferrer, and J. I. Cerdá, Phys. Rev. B **104**, 195104 (2021).
[35]P. Rivero, V. M. García-Suárez, D. Pereñiguez, K. Utt, Y. Yang, L. Bellaiche, K. Park, J. Ferrer, and S. Barraza-Lopez, Comput. Mater. Sci. **98**, 372 (2015).

[36]G. Martínez-Carracedo, L. Oroszlány, A. García-Fuente, B. Nyári, L. Udvardi, L. Szunyogh, and J. Ferrer, Phys. Rev. B **108**, 214418 (2023).
[37]A. Baumgärtner, A. Burkitt, D. Ceperley, H. De Raedt, A. Ferrenberg, D. Heermann, H. Herrmann, D. Landau, D. Levesque, W. von der Linden *et al.*, *The Monte Carlo Method in Condensed Matter Physics* (Springer Science & Business Media, 2012), Vol. 71.
[38]Z. Sun, G. Ye, C. Zhou, M. Huang, N. Huang, X. Xu, Q. Li, G. Zheng, Z. Ye, C. Nnokwe *et al.*, Nat. Phys. **20**, 1764 (2024).
[39]X. Lu, X. Wu, and H. Xiang, Phys. Rev. B **91**, 100405 (2015).
[40]A. I. Liechtenstein, M. I. Katsnelson, V. P. Antropov, and V. A. Gubanov, J. Magn. Magn. Mater. **67**, 65 (1987).
[41]C. Boix-Constant, A. Rybakov, C. Miranda-Pérez, G. Martínez-Carracedo, J. Ferrer, S. Mañas-Valero, and E. Coronado, Adv. Mater. **37**, 2415774 (2025).
[42]D. Bennett, G. Martínez-Carracedo, X. He, J. Ferrer, P. Ghosez, R. Comin, and E. Kaxiras, Phys. Rev. Lett. **133**, 246703 (2024).
[43]G. Martínez-Carracedo, A. García-Fuente, L. Oroszlány, L. Szunyogh, and J. Ferrer, Phys. Rev. B **110**, 184406 (2024).
[44]G. Martínez-Carracedo, L. Oroszlány, A. García-Fuente, L. Szunyogh, and J. Ferrer, Phys. Rev. B **107**, 035432 (2023).
[45]T. Wimmer, A. Kamra, J. Gückelhorn, M. Opel, S. Geprägs, R. Gross, H. Huebl, and M. Althammer, "Observation of antiferromagnetic magnon pseudospin dynamics and the Hanle effect," Phys. Rev. Lett. **125**, 247204 (2020).
[46]J. Gückelhorn, S. de-la Peña, M. Scheufele, M. Grammer, M. Opel, S. Geprägs, J. C. Cuevas, R. Gross, H. Huebl, A. Kamra *et al.*, "Observation of the nonreciprocal magnon Hanle effect," Phys. Rev. Lett. **130**, 216703 (2023).
[47]P. Tang and G. E. W. Bauer, "Electrical injection and transport of coherent magnons in non-collinear antiferromagnets," arXiv:2312.09694 (2025).
[48]R. Das and R. den Teuling (2025). "Dispersion in $NiPS_3$," Zenodo. https://doi.org/10.5281/zenodo.17532238.
[49]J. Ferrer (2025). "DFT and Monte Carlo results for monolayer $NiPS_3$," Zenodo. https://doi.org/10.5281/zenodo.17529866.
[50]S. Streib, N. Vidal-Silva, K. Shen, and G. E. W. Bauer, Phys. Rev. B **99**, 184442 (2019).
[51]R. White, M. Sparks, and I. Ortenburger, Phys. Rev. **139**, A450 (1965).
[52]A. S. Sukhanov, O. Utesov, A. Korshunov, N. Andriushin, M. Pavlovskii, S. Nikitin, A. Kulbakov, K. Manna, C. Felser, and M. C. Rahn, Phys. Rev. Lett. **135**, 086703 (2025).
[53]D. Jana, D. Vaclavkova, R. K. Ulaganathan, R. Sankar, M. Orlita, C. Faugeras, M. Koperski, M. E. Zhitomirsky, and M. Potemski, Phys. Rev. B **112**, 165427 (2025).
[54]T. P. Lyons, J. Puebla, K. Yamamoto, R. S. Deacon, Y. Hwang, K. Ishibashi, S. Maekawa, and Y. Otani, Phys. Rev. Lett. **131**, 196701 (2023).
[55]X. Zhang, C.-L. Zou, L. Jiang, and H. X. Tang, Sci. Adv. **2**, e1501286 (2016).
[56]C. A. Potts, E. Varga, V. A. Bittencourt, S. V. Kusminskiy, and J. P. Davis, Phys. Rev. X **11**, 031053 (2021).